

Finite Difference Modeling of Attenuation and Anisotropy

Mary L. Krasovec, Daniel R. Burns, and M. Nafi Toksöz
Earth Resources Laboratory
Dept. of Earth, Atmospheric, and Planetary Sciences
Massachusetts Institute of Technology
Cambridge, MA 02139

Abstract

A finite difference scheme which includes the effects of attenuation and anisotropy is tested for seismic reflection and borehole acoustic models. The validity of the scheme is established using a 3D homogenous isotropic model to compare results to the discrete wavenumber method. Three models are then investigated. First, reflections from a 3D flat layered model are analyzed for offset and azimuthal dependence of attenuation. Second, discrete fractures are included in a 2D flat layered model to examine their effect on reservoir top and bottom reflections. Third, a 3D borehole in both hard and soft formations is modeled to test the effect of attenuation on guided waves.

1 Introduction

Since attenuation is an important property of the subsurface, there is a need for models of seismic wave propagation in heterogenous attenuating media. Although previously available methods, such as the discrete wavenumber method (Bouchon, 1981) can handle attenuation, they are limited in the types of models that can be represented.

For one topic of interest, the characterization of fractured media, common indicators of the presence of fractures include velocity anisotropy, shear wave splitting, and AVO effects. It is less common to use attenuation because it can be difficult to measure, and the relationship between fracture set properties and attenuation is complicated. However, it is clear that fractures have an effect on the attenuation of a medium (Walsh, 1966), suggesting that attenuation information could aid in delineating fractured reservoirs.

Borehole guided waves can be used to estimate formation properties and stress regime (Huang, 2003), but such guided waves are affected by attenuation in the formation and the borehole fluid.

Physical models of attenuation are derived in Walsh (1966) and O'Connell and Budiansky (1977), among others. There have been many papers presenting laboratory attenuation measurements, including Toksöz et al. (1979), Winkler and Nur (1979), and Winkler et al. (1979). Numerical viscoelastic finite difference schemes have been developed, such as Day and Minster (1984) which used a Padé approximation to model the attenuation. The methods of Emmerich and Korn (1987) and Blanch et al. (1995) improve on the accuracy and computational efficiency of the Padé approximation. Carcione (1993) simulates the response of linear isotropic-anelastic media, and Robertsson et al. (1994) contains a detailed study of the stability, accuracy, numerical dispersion, physical dispersion, and computational efficiency of their viscoelastic finite difference scheme.

In an effort to expand the modeling tools available at ERL, we have updated a finite difference code written by Cheng (1994) to model seismic waves in anisotropic, viscoelastic media. Originally written in Fortran, the code has been converted to MPI C to allow it to run large models on a PC cluster. A front end graphic user interface has also been developed to make the code easier to use.

Our focus in this paper is on establishing the validity of the finite difference forward modeling scheme by testing it on various models. The paper has two sections: the first discusses briefly the modeling method and the data processing steps. The second section goes through three applications of the finite difference scheme: a 3D flat reflector model, a 2D flat reflector model with discrete fractures, and a borehole model.

2 Method

2.1 The Forward Modeling method

We use a finite difference algorithm originally developed at ERL (Cheng, 1994). It is 2nd order in time and 4th order in space, and models anisotropy with up to nine elastic constants. The wave equation is formulated in velocity and stress, and discretized on a staggered grid.

The code was originally developed in Fortran, and has been converted to MPI C so that large models can be run on computer clusters. It has also been updated to allow a choice between the boundary conditions of Cerjan et al. (1987) or the original boundary conditions (Higdon, 1986, 1987).

The method of Emmerich and Korn (1987) is used to include attenuation in the calculations, with three relaxation frequencies. The approximation of the attenuation value is shown in Figure 1 for Q values of 100 and 20. The approximation is best in the range from a few Hertz to about 70 Hertz. The reflector finite difference models in this paper use wavelets centered at 30 and 40 Hertz, which are both in the range of good approximation. The borehole model uses a 7 kHz wavelet, with the reference frequencies shifted appropriately to achieve a good approximation of the attenuation value within that frequency band.

Figure 2 shows the wavelet shape after it has traveled 5 wavelengths. Results from two methods are compared: the finite difference result and the solution from the discrete wavenumber method of Bouchon (1981). The approximation for Q=100 is quite good; for Q=20 it shows more error, which is expected since the attenuation estimation fails at very low and very high frequencies.

The example presented in Section 3.1 was originally run for comparison to discrete wavenumber results, and so uses a Ricker wavelet at 30 Hertz. The example in Section 3.2 uses a 40 Hertz Kelly wavelet. The borehole example in Section 3.3 uses a 7 kHz Kelly wavelet.

2.2 Data Processing

In analyzing the synthetic data from seismic reflection models, the following steps are used:

1. Calculate NMO times, where the NMO velocities take into account dispersion (using the velocity at the source peak frequency) and effective medium properties, if necessary.
2. Time shift to align the wavelets.
3. Window appropriately. We use a rectangular window, with a Blackman window to taper the edges.
4. Zero pad to increase the sampling of the Fourier transform.
5. Calculate the spectrum of the wavelet as the absolute value of the fast Fourier transform.
6. Attenuation estimates are calculated from the interval top and bottom spectra, as discussed in Section 2.3.

2.3 Q Estimation

We use the spectral ratio method to estimate Q, following the notation of Alshammery (1998), with the exception that we use frequency f rather than angular frequency ω . $A_n(f)$ is the amplitude spectrum of a direct arrival at some distance d_n from the source, and $A_1(f)$ is the spectrum of the arrival at some nearer reference distance d_1 . The log of their ratio

$$\delta(f) = \log A_1(f)/A_n(f) \quad (1)$$

can be fit to a straight line

$$\delta_{fit}(f) = mf + \delta_0. \quad (2)$$

The slope m of this line relates to the Q value of the medium, the distance traveled $d_n - d_1$, and the background velocity c as follows:

$$Q = \frac{\pi(d_n - d_1)}{mc} \quad (3)$$

In order to estimate interval Q from reflection data, the compared spectra are those of the reflection events from the top and bottom of the interval. In this case, Alshammery (1998) replaces $(d_n - d_1)/c$ in Equation 3 by Δt , the time spent in the interval by the bottom reflected wave (White, 1992).

$$Q = \frac{\pi \Delta t}{m}. \quad (4)$$

Like Alshammery (1998), we use a ray tracing algorithm to estimate Δt .

3 Synthetic Data Examples

Three different model types are investigated, as listed in Table 1.

3.1 Interval Q estimation

We test the effects of interval Q using a three layer reservoir model, shown in Figure 3. The top and bottom layers are a background material, the middle layer is the reservoir.

We run three variations on the model by adjusting the reservoir Q value Q_{res} , the background Q value Q_o , and also by adding vertically aligned fractures to the reservoir layer. The parameters of the models are listed in Table 1.

To model the presence of fractures, we use an effective velocity model based on the crack compliances of Schoenberg and Douma (1988), as discussed in Krasovec et al. (1998). The model allows for one set of aligned fractures, which we assume to be horizontal and aligned parallel to the y axis. The fracture set is defined by a crack density value, a crack aspect ratio, and the compressibility of the pore fluid, which for this study we assume to be 0.

The effect of the fractures is shown in Figure 4. We use an aspect ratio of .1, which results in a fracture set porosity of 4.2% and a high degree of anisotropy: 20% for the P-wave velocity. Note that since the density is slightly lowered by the fracture set, the effective shear wave velocity in the crack normal direction (angle 0) actually increases slightly.

Figures 5, 6, and 7 show the synthetic data for the three models, as well as the NMO corrected events and their spectra. The trace scales on the wiggle plots and the colorlimits on the spectra plots are the same for each of three figures. Only the receivers located on the x axis (crack normal) are shown. The top reflector shows a polarity change because of the extremity of the change in the elastic constants caused by the fracture set.

The effect of the attenuation can be seen in the amplitudes of the reflected events in Figures 6 and 7. The bottom shear reflection, which is at traveltime 650 msec for the furthest offset trace, is barely visible in Figure 7. The amplitude of the P reflections can be compared in the spectra plots: the top reflector shows a slight decrease in energy due to the attenuation, while the decrease in the bottom reflector energy is more pronounced.

The attenuation also broadens the reflection events. The peak frequency of the spectrum at zero offset for the elastic model is 38.2 Hertz, but 32.9 Hertz for the attenuated model.

Figure 8 shows the interval Q value estimated from the top and bottom reflector spectra. The top plot shows the Q estimation for model B1, where the interval has $Q=20$ and the overburden has $Q=100$; The Q value at zero offset is underestimated, which agrees with the findings of Alshammery (1998), who estimated interval Q values from discrete wavenumber reflection data. The misfit is likely due to the limited bandwidth of the source.

The Q estimation for model B2 is not plotted, as there is no attenuation in the model.

In the bottom plot of Figure 8, results for Model B3 are shown. The values are similar to those found in the isotropic case, except at far offsets where there is a polarity change in the interval top reflector in the crack normal direction. This polarity change causes the spectrum of the wavelet to go to zero, and the Q estimation to be unstable.

3.2 Effective attenuation from discrete fractures

The next example puts discrete fractures into a 2D layered model. Pearce (2003) uses similar models, but runs them in 3D and looks at the dependence of the scattered wavefield on the fracture set characteristics. Our approach is to investigate the effects which discrete fractures have on reflection events.

The discrete fractures are modeled as columns of grid elements which have altered elastic constants (Daley et al., 2002). These columns could be thought of as highly fractured zones.

The model is run in 2D so that the grid can be very finely sampled (.5 meters) and the discrete fractures can have spacing much smaller than the seismic wavelength. We compare the results of regularly spaced to randomly spaced fractures, as well as adding background attenuation to the model. The background material properties are listed in Table 1.

The geometry of the model with irregularly spaced fractures is shown in Figure 9. The bottom plot shows a histogram of the fracture spacings. The spacing has a mean of 2 meters, matching the fracture spacing in the regularly spaced model so that the total number of fractures in the two cases is the same. The fracture spacing was generated by sampling a random process, using a correlation length of 1 so that the space between any two fractures was independent of the neighboring spacings. The spacing values are rounded to the nearest multiple of the grid spacing. This results in a large number of .5 spaced fractures, because anything less than .5 had to be rounded up.

Figure 10 shows the data in the case of no discrete fractures, with and without attenuation. The bright events with zero offset arrival times of 330 ms and 410 ms are the P wave reflections from the top and bottom of the reservoir. The two later events which increase amplitude with offset are the converted wave reflections off the top and bottom of the reservoir. They have times of about 550 and 620 for the furthest offset traces. Other visible events are interbed multiples.

Figure 11 shows the data from the model with regularly spaced discrete fractures. Compared to Figure 10, all events show slightly different amplitudes. In addition, the traveltimes of the reservoir bottom reflections are later because the waves are traveling through the fractures. The reservoir bottom P reflection and the reservoir top S reflector overlap at far offsets.

Figure 12 shows the data in the case of irregularly spacing discrete fractures, with and without attenuation. The reflection events in these gathers are similar to those in Figure 11, but the irregular spacing of the fractures causes low amplitude scattering at later times.

So what we can see in these examples is that the discrete fractures at such a close spacing have two effects. First, both the regular and irregular fracture distributions act as an effective medium, lowering the material velocity in the fractured layer. The second effect happens only for the case with irregular fractures: regions of more sparsely or densely spaced fractures cause scattering.

3.3 Attenuation in an empty borehole

Figure 13 shows the model geometry for the empty borehole models. The borehole radius is .1 meters. The source is centered in the borehole.

Figure 14 shows the synthetic data for the hard formation, with and without attenuation. The P, pseudo-Rayleigh, and Stoneley waves are visible. All three arrivals are still present in the traces from the attenuating model, but high frequencies and the Stoneley wave have been greatly reduced by the attenuation.

The effect of attenuation is more drastic in the soft formation, as the lower velocity means more cycles per unit length. Figure 15 shows the synthetic data for the soft formation, with and without attenuation. The bottom plot has the amplitude scaled by a factor of 4 so that the events are visible. Again the Stoneley wave is greatly reduced by the attenuation.

4 Conclusions

The formulation of Emmerich and Korn (1987) for modeling attenuation in 3D finite difference models works reasonably well for a wide range of models. This will provide an additional tool for fracture characterization, in the form of interval attenuation estimates. It will also allow for more realistic simulations of borehole guided wave applications.

5 Acknowledgments

This work was supported by the Earth Resources Laboratory Founding Members, the Department of Energy grant number DE-FC26-02NT15346, and by ENI S.p.A. AGIP.

References

- Alshammery, H. J. (1998). Interval attenuation estimation. Master's thesis, Massachusetts Institute of Technology.
- Blanch, J. O., Robertsson, J. O. A., and Symes, W. W. (1995). Modeling of a constant Q: Methodology and algorithm for an efficient and optimally inexpensive viscoelastic technique. *Geophysics*, 60(01):176–184.
- Bouchon, M. (1981). A simple method to calculate Green's functions in elastic layered media. *BSSA*, 71(4):959–971.
- Carcione, J. M. (1993). Seismic modeling in viscoelastic media. *Geophysics*, 58:110–120.
- Cerjan, C., Kosloff, D., Kosloff, R., and Reshef, M. (1987). A nonreflecting boundary condition for discrete acoustic and elastic wave equations. *Geophysics*, 50(4):705–708.
- Cheng, N. (1994). *Borehole Wave Propagation in Isotropic and Anisotropic Media: Three-Dimensional Finite Difference Approach*. PhD thesis, Massachusetts Institute of Technology.
- Daley, T. M., Nihei, K. T., Myer, L. R., Majer, E. L., Queen, J. H., Fortuna, M., Murphy, J., and Coates, R. T. (2002). Numerical modeling of scattering from discrete fractures zones in a San Juan Basin gas reservoir. In *72nd Ann. Internat. Mtg: Soc. of Expl. Geophys.*
- Day, S. M. and Minster, J. B. (1984). Numerical simulation of attenuated wavefields using a Padé approximant method. *Geophys. J. R. Astr. Soc.*, 78:105–118.
- Emmerich, H. and Korn, M. (1987). Incorporation of attenuation into time-domain computations of seismic wave fields. *Geophysics*, 52(9):1252–1264.
- Higdon, R. L. (1986). Absorbing boundary conditions for difference approximations to the multi-dimensional wave equation. *Mathematics of Computation*, 47:437–459.
- Higdon, R. L. (1987). Numerical absorbing boundary conditions for elastic wave propagation. *Mathematics of Computation*, 49:65–90.
- Huang, X. (2003). *Effects of tool positions on borehole acoustic measurements: a stretched grid finite difference approach*. PhD thesis, Massachusetts Institute of Technology.
- Krasovec, M. L., Rodi, W., and Toksoz, M. N. (1998). *Sensitivity analysis of amplitude variation with offset (AVO) in fractured media*, pages 201–203. Soc. of Expl. Geophys.
- O'Connell, R. J. and Budiansky, B. (1977). Viscoelastic properties of fluid-saturated cracked solids. *J. Geophys. Res.*, 82:5719–5735.
- Pearce, F. (2003). Spectral analysis of scattered waves in fractured reservoirs. In *MIT-ERL Reservoir Delineation Consortium Report*.
- Robertsson, J. O. A., Blanch, J. O., and Symes, W. (1994). Viscoelastic finite-difference modeling. *Geophysics*, 59(9):1444–1456.
- Schoenberg, M. and Douma, J. (1988). Elastic-wave propagation in media with parallel fractures and aligned cracks. *Geophys. Prosp.*, 36(06):571–590.

- Toksöz, M. N., Johnston, D. H., and Timur, A. (1979). Attenuation of seismic waves in dry and saturated rocks: I. laboratory measurements. *Geophysics*, 44(4):681-690.
- Walsh, J. B. (1966). Seismic attenuation in rock due to friction. *J. Geophys. Res.*, 71:2591-2599.
- White, R. E. (1992). The accuracy of estimating Q from seismic data. *Geophysics*, 57(11):1508-1511.
- Winkler, K. and Nur, A. (1979). Pore fluids and seismic attenuation in rocks. *Geophys. Res. Lett.*, 6:1-4.
- Winkler, K., Nur, A., and Gladwin, M. (1979). Friction and seismic attenuation in rocks. *Nature*, 277:528-531.

A. 3D Layered Models (Figure 3)

Model	α_{bk}	β_{bk}	ρ_{bk}	α_{res}	β_{res}	ρ_{res}	Q_{bk}	Q_{res}	fracture density
A1	5	2.78	2.7	4.5	2.5	2.6	100	20	0
A2	5	2.78	2.7	4.5	2.5	2.6	10000	10000	0.1
A3	5	2.78	2.7	4.5	2.5	2.6	100	20	0.1

B. 2D Discrete fracture models (Figure 9)

Model	α_{bk}	β_{bk}	ρ_{bk}	α_{res}	β_{res}	ρ_{res}	Q^*	fracture spacing
B1	4	2.353	2.3	3	1.765	2.2	10000	no fractures
B2	4	2.353	2.3	3	1.765	2.2	100	no fractures
B3	4	2.353	2.3	3	1.765	2.2	10000	regular
B4	4	2.353	2.3	3	1.765	2.2	100	irregular
B5	4	2.353	2.3	3	1.765	2.2	10000	regular
B6	4	2.353	2.3	3	1.765	2.2	100	irregular

*background and reservoir have the same Q.

C. Empty borehole models (Figure 13)

Model	α_{fm}	β_{fm}	ρ_{fm}	Q_{fm}	α_{fl}	ρ_{fl}	Q_{fl}
C1 (hard)	4	2.3	2.3	-	1.5	1.0	-
C2 (hard)	4	2.3	2.3	40	1.5	1.0	10
C3 (soft)	2	1.15	1.6	-	1.5	1.0	-
C4 (soft)	2	1.15	1.6	40	1.5	1.0	10

Table 1: Model parameters. The indicated figures show the model geometries. Unspecified attenuation values (-) mean a non-attenuating version of the code was used.

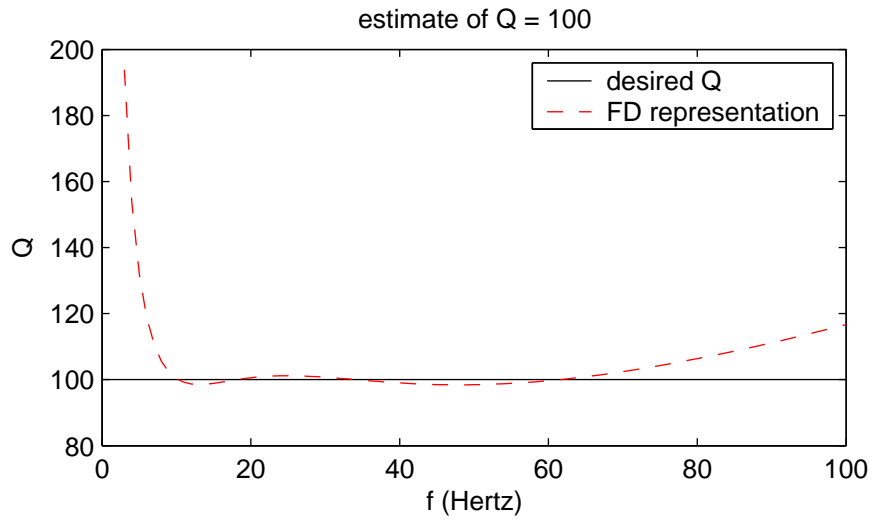
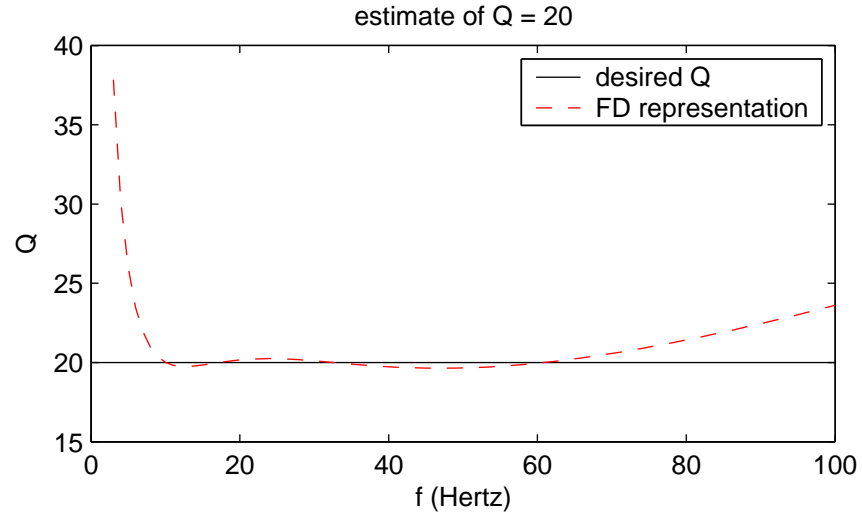


Figure 1: Estimation of Q for the finite difference code, used for the flat layered models A1-A3 and B1-B6.

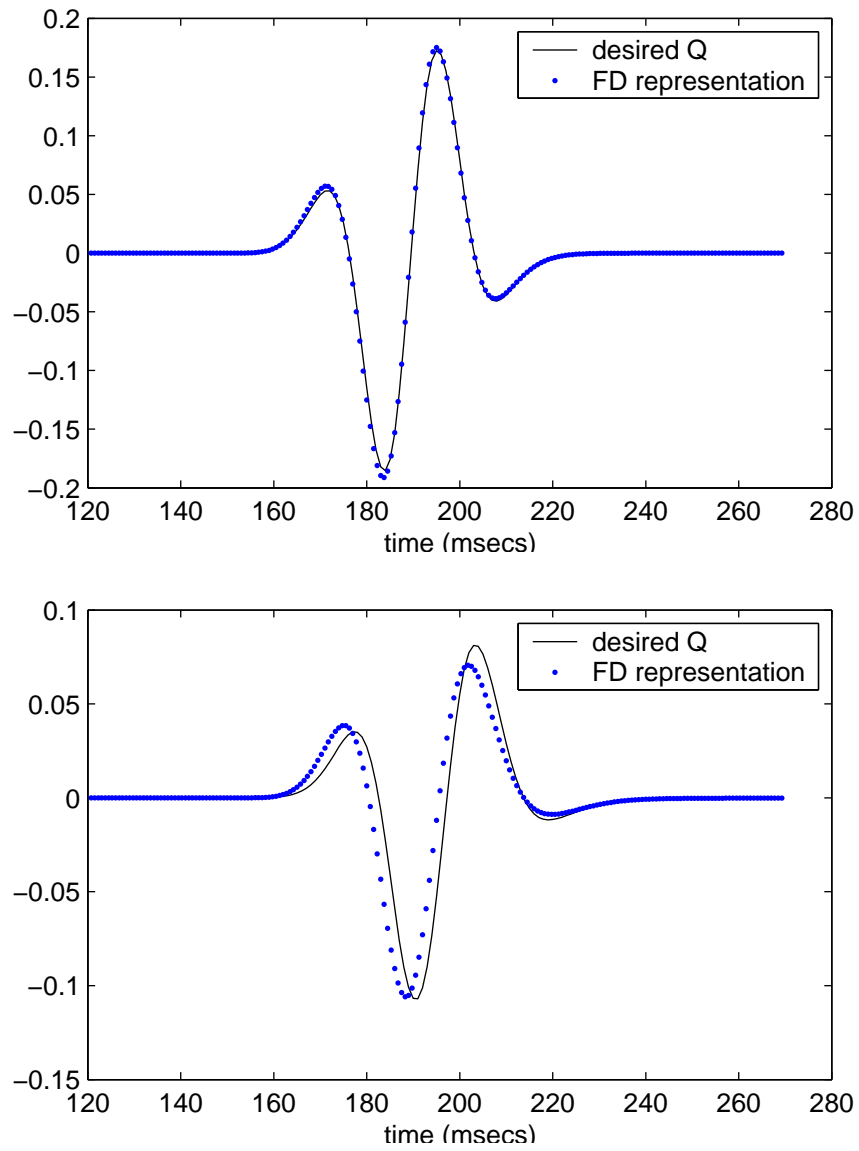


Figure 2: Comparison of finite difference and discrete wavenumber results. The top plot is for a Q value of 100, the bottom for Q=20.

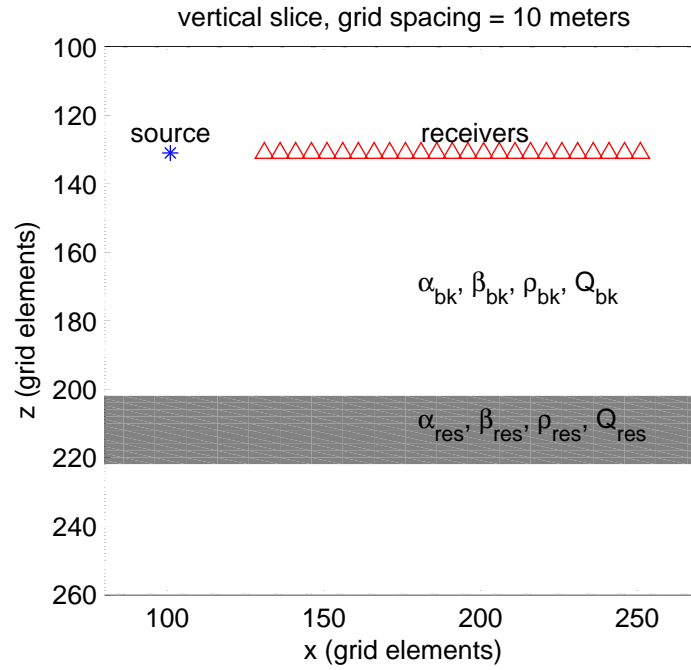


Figure 3: Geometry of 3D reservoir models A1-A3. The material properties are listed in Table 1.

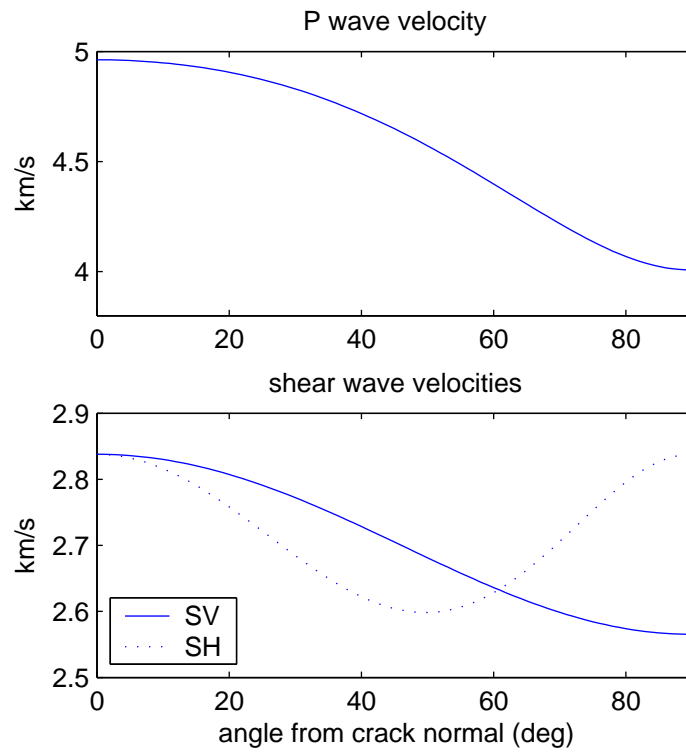


Figure 4: Effective velocities due to the presence of aligned vertical fractures in the reservoir layer in Models A2 and A3.

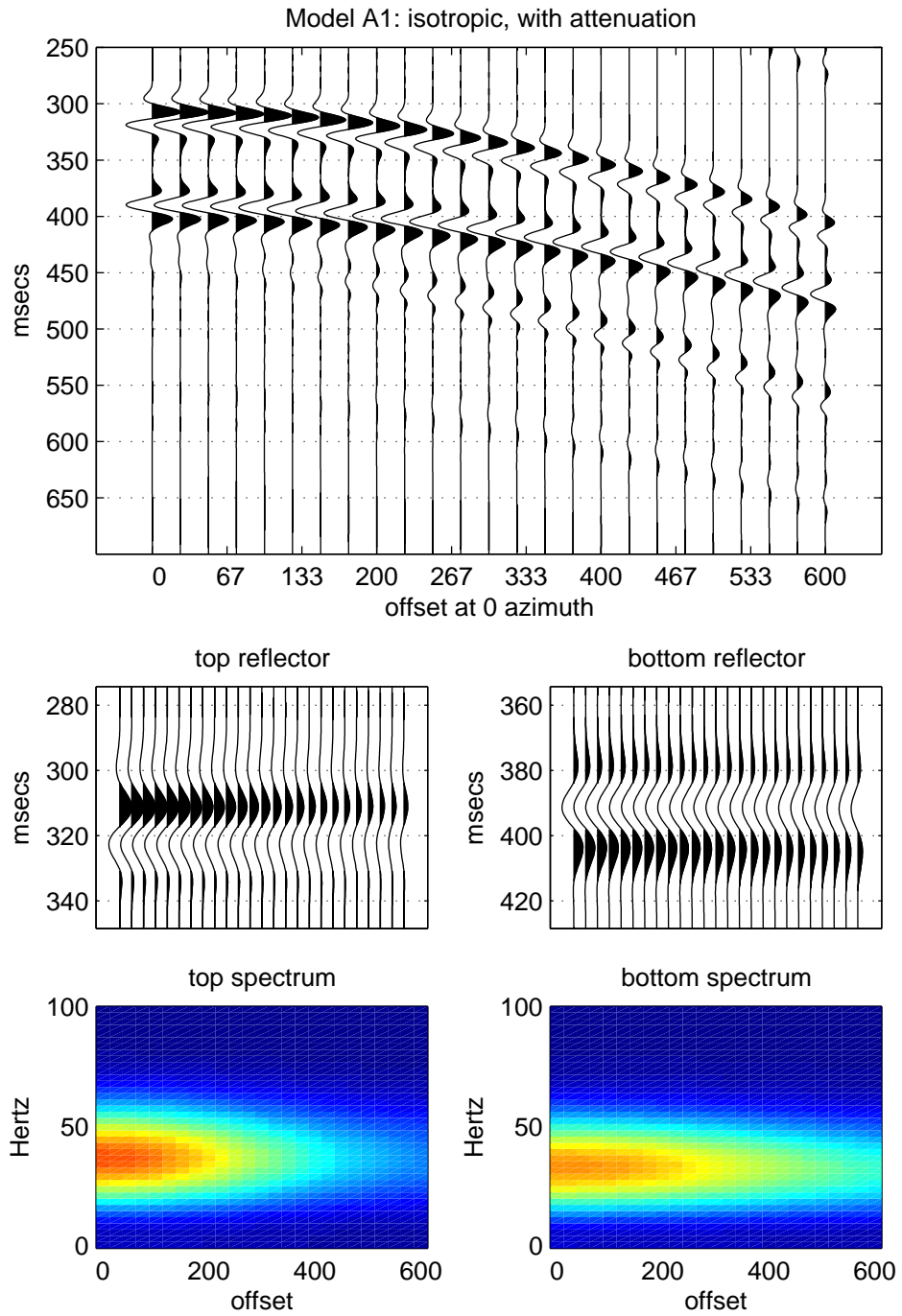


Figure 5: Synthetic data and spectra for Model A1. Model parameters are listed in Table 1. The traces shown are for receivers on the x axis, which is the crack normal direction.

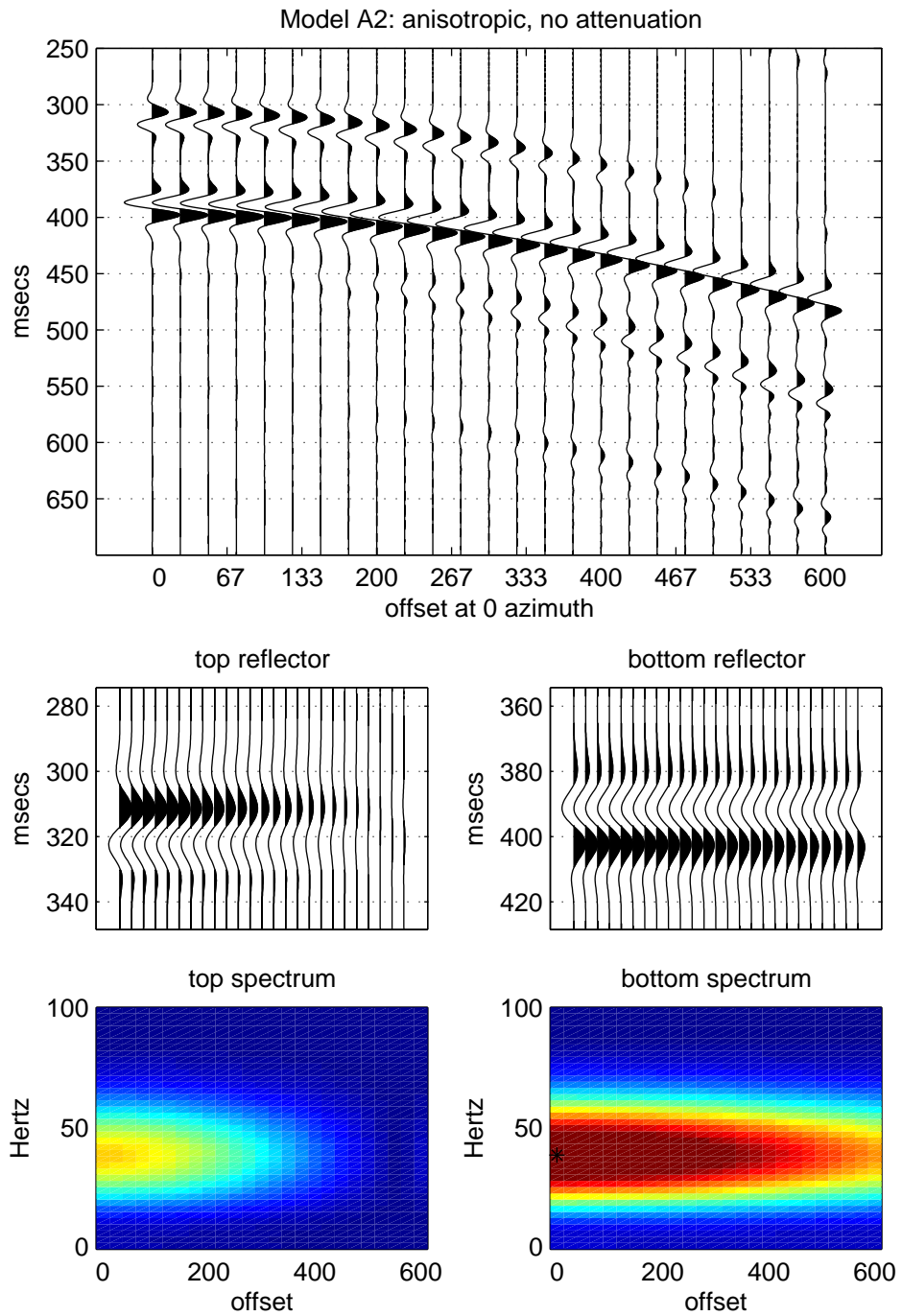


Figure 6: Synthetic data and spectra for Model A2. Model parameters are listed in Table 1. The traces shown are for receivers on the x axis, which is the crack normal direction. The black asterisk on the bottom spectrum plot is at the maximum of the zero offset spectrum, which is at 38.2 Hertz.

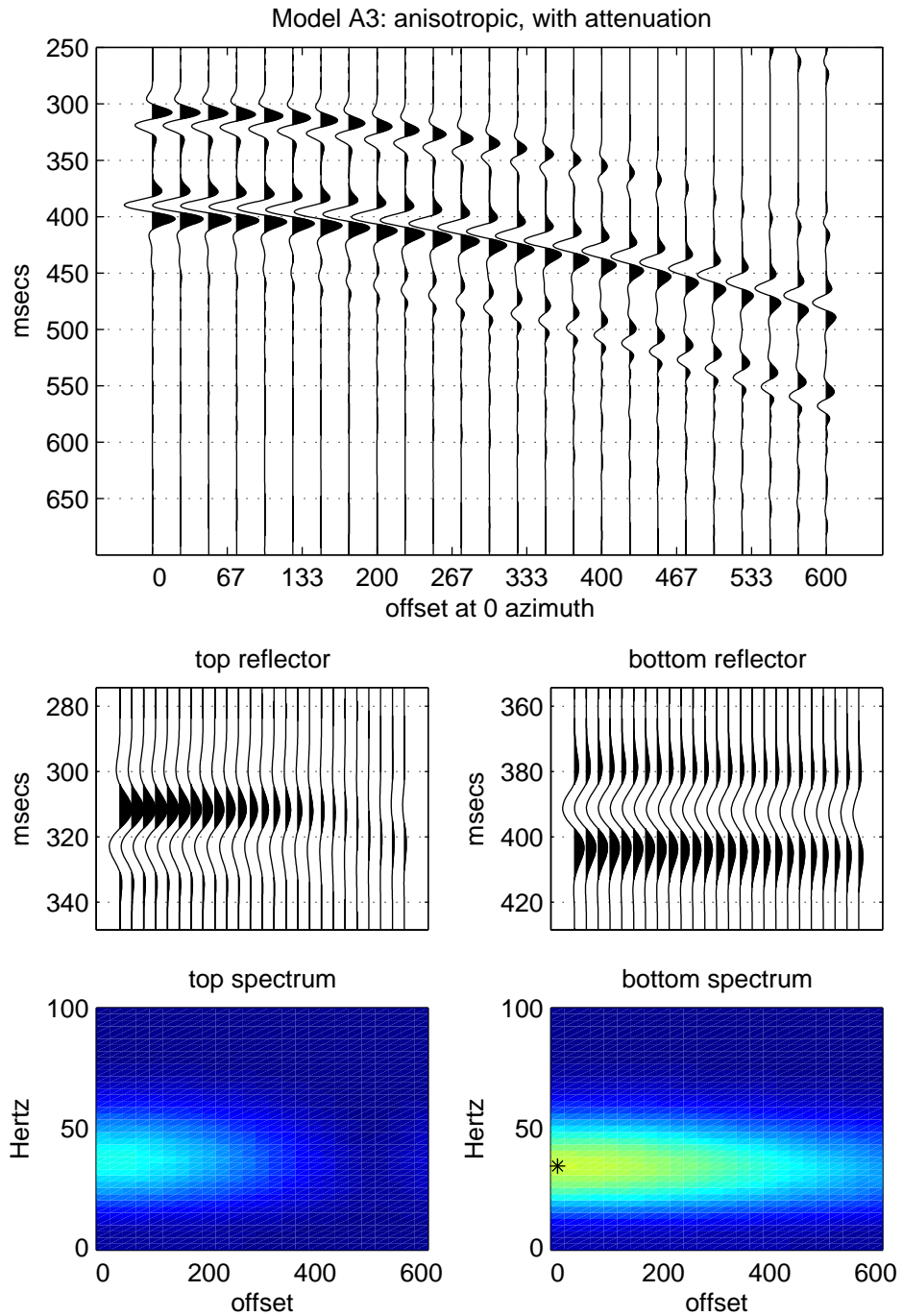


Figure 7: Synthetic data and spectra for Model A3. Model parameters are listed in Table 1. The traces shown are for receivers on the x axis, which is the crack normal direction. The black asterisk on the bottom spectrum plot is at the maximum of the zero offset spectrum, which is at 32.9 Hertz, a reduction by 13% from the nonattenuating case.

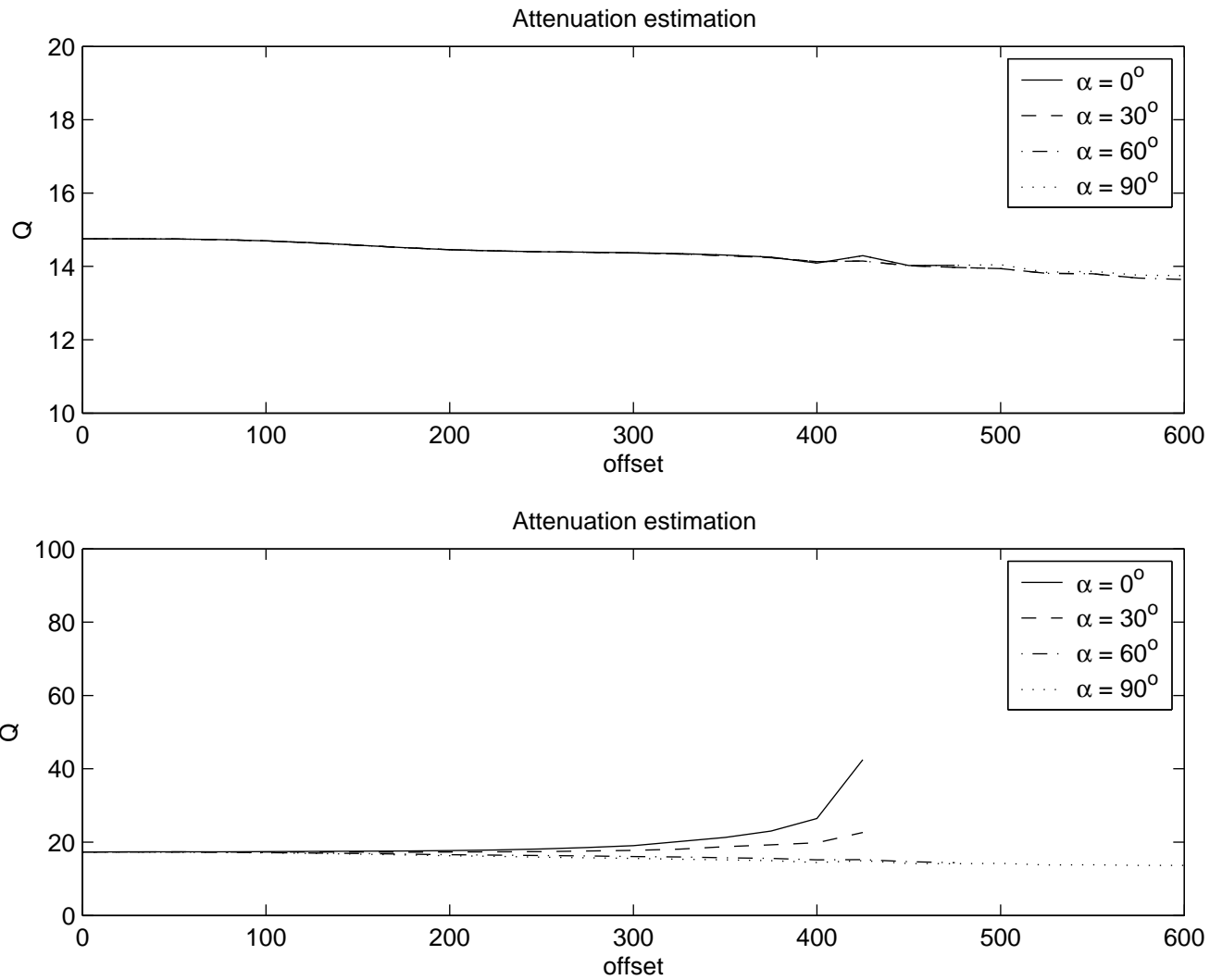


Figure 8: Interval Q estimations from the data in Figures 5 and 7. The Q estimation is cut off near where the polarity of the reflection reverses, at about offset 425 meters in the azimuth 0 and 30 directions.

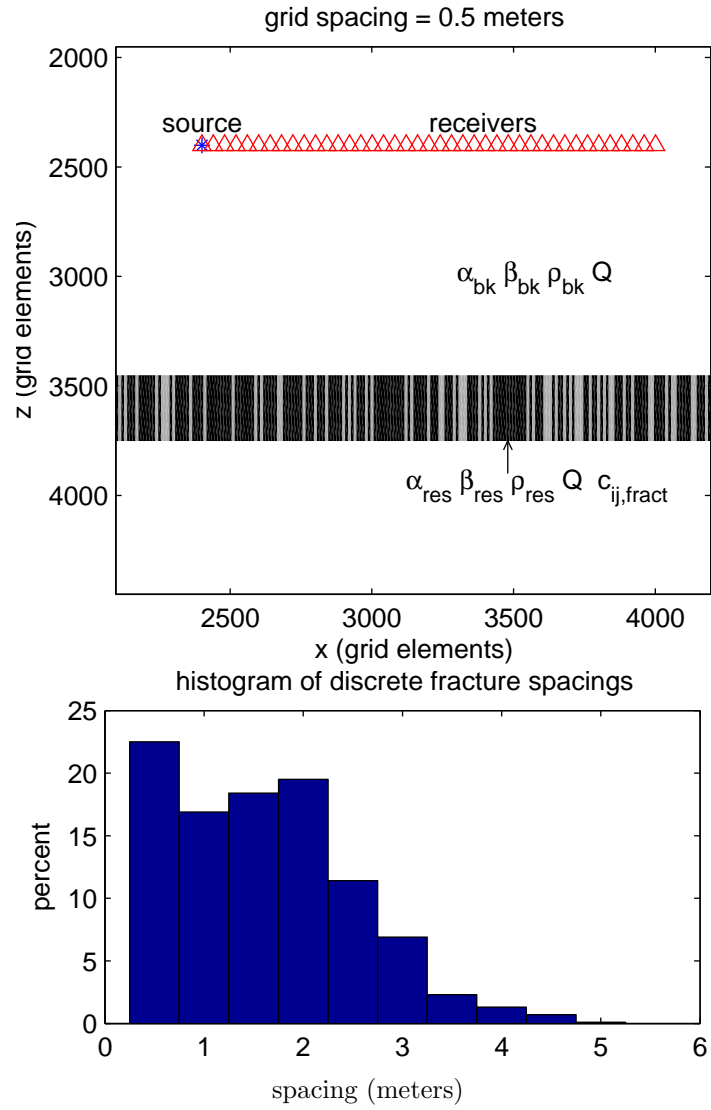


Figure 9: Geometry of 2D discrete fracture models B1-B6. Attenuating models have the same value of Q for all materials, as listed in Table 1. The random distribution of discrete fractures (vertical gray lines in the middle layer) is for models B5 and B6.

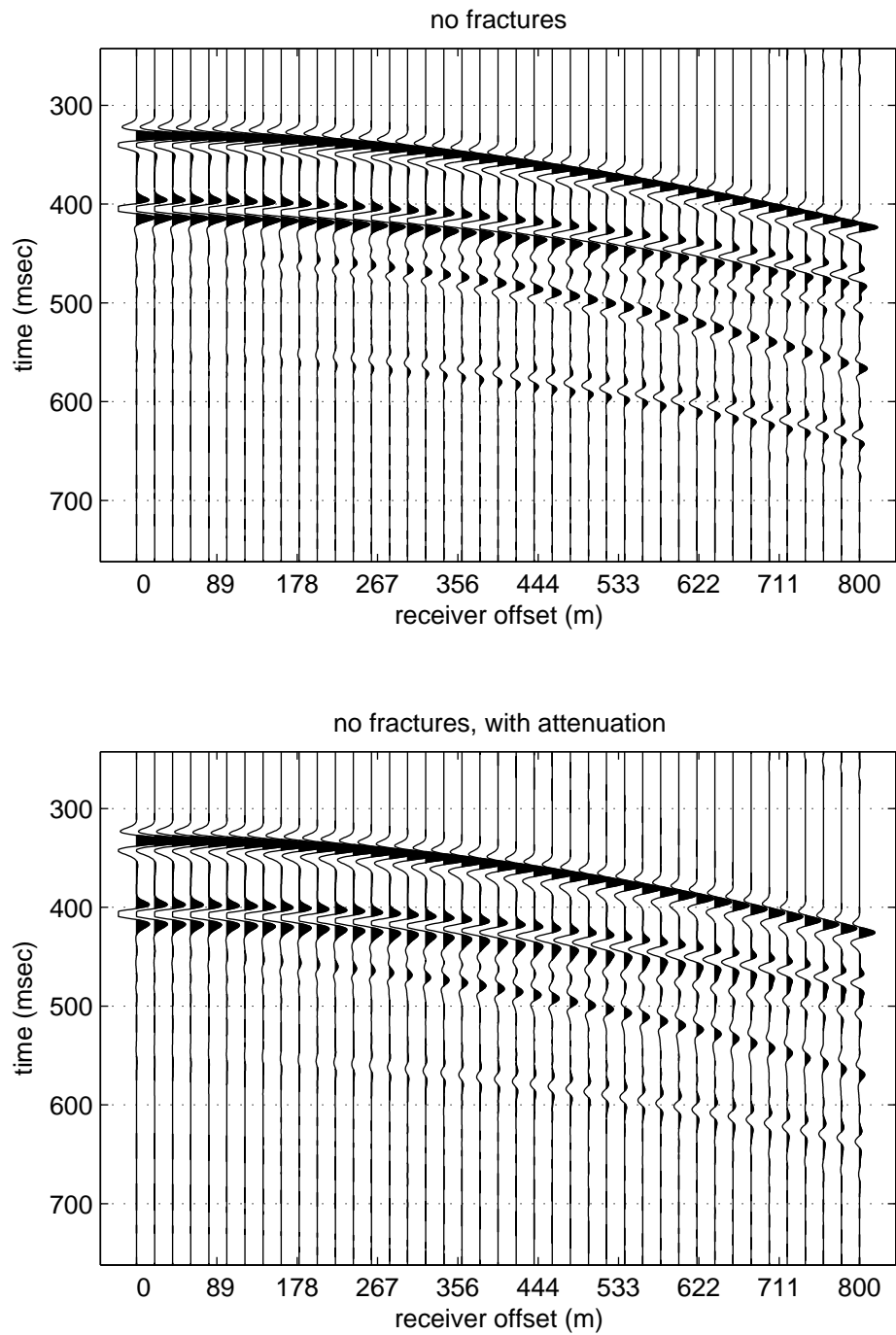


Figure 10: Synthetic data for models B1 and B2: the 2D reservoir model with no discrete fractures, with and without attenuation.

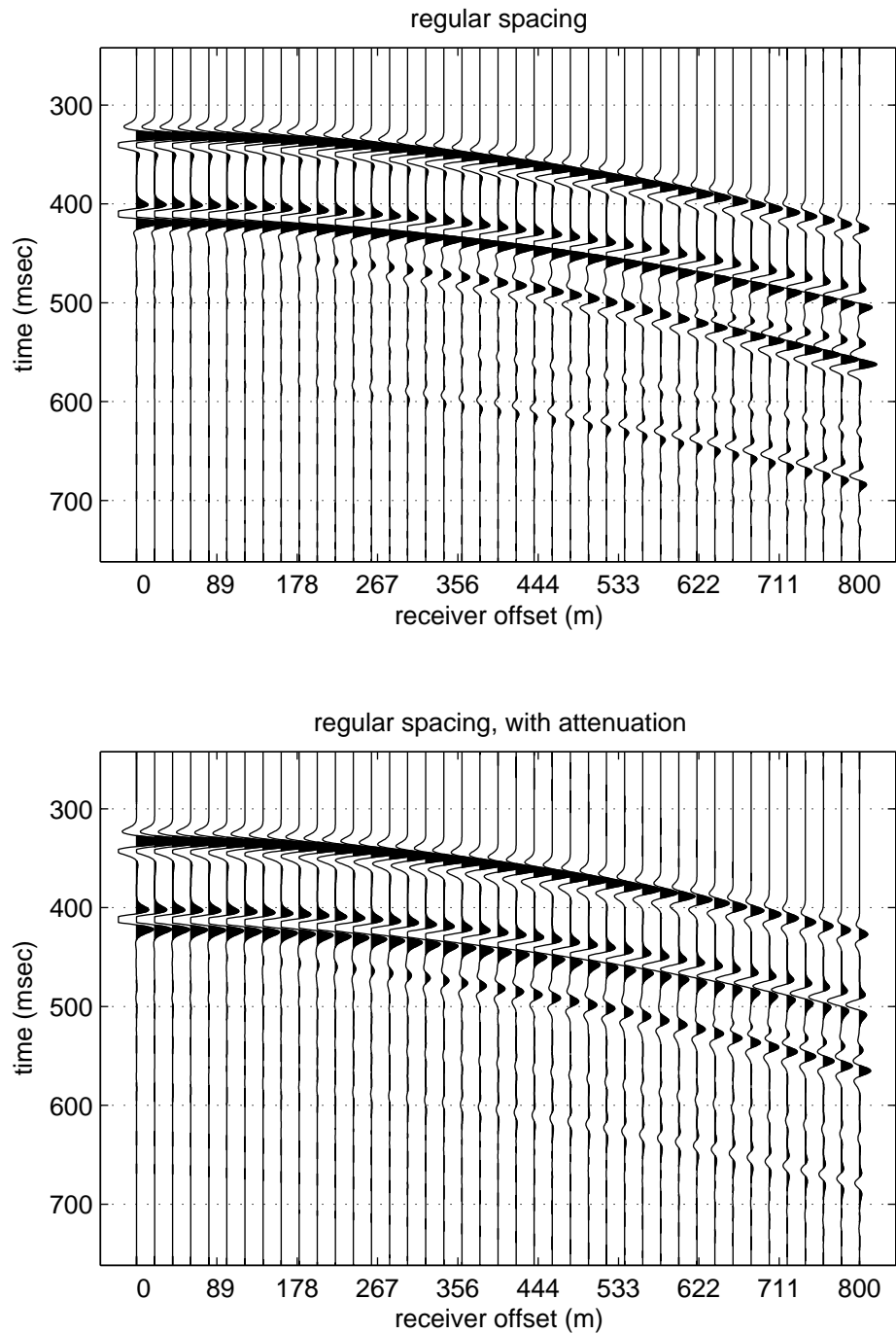


Figure 11: Synthetic data for models B3 and B4: the 2D reservoir model with regularly spaced discrete fractures, with and without attenuation. The grid spacing is .5 meters, the fracture spacing is 2 meters, and the seismic wavelength is 75 meters. Compared to Figure 10, the regularly spaced fractures act as an effective medium, delaying the reflections from the reservoir bottom. There is no visible scattered wavefield.

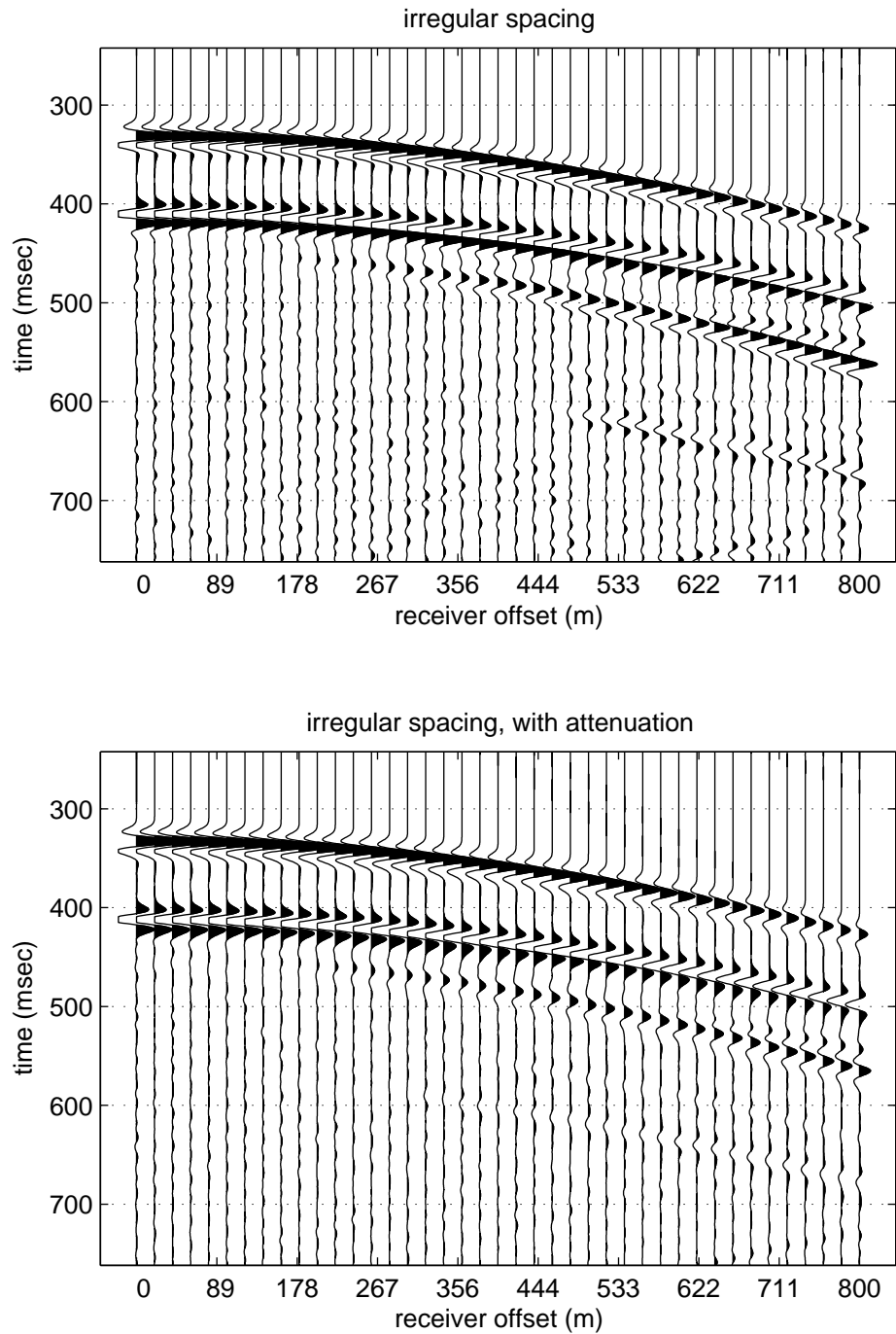


Figure 12: Synthetic data for models B5 and B6: the 2D reservoir model with irregularly spaced discrete fractures; the fracture spacing has a mean value of 2 meters. In addition to the reflection events seen in Figures 10 and 11, there is also a scattered field visible at later times. These are waves scattered off regions of tightly or sparsely spaced fractures.

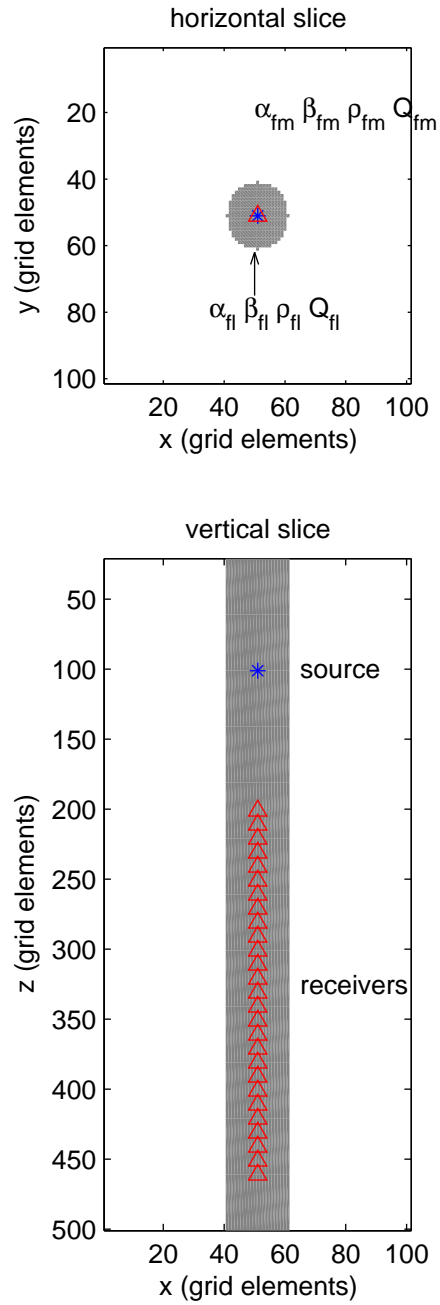


Figure 13: Empty borehole model geometry for models C1 through C4. The white is fluid, the black is formation. The borehole radius is .1 m, and the material properties are given in Table 1. The blue asterisk is the source position, the triangles are the receivers.

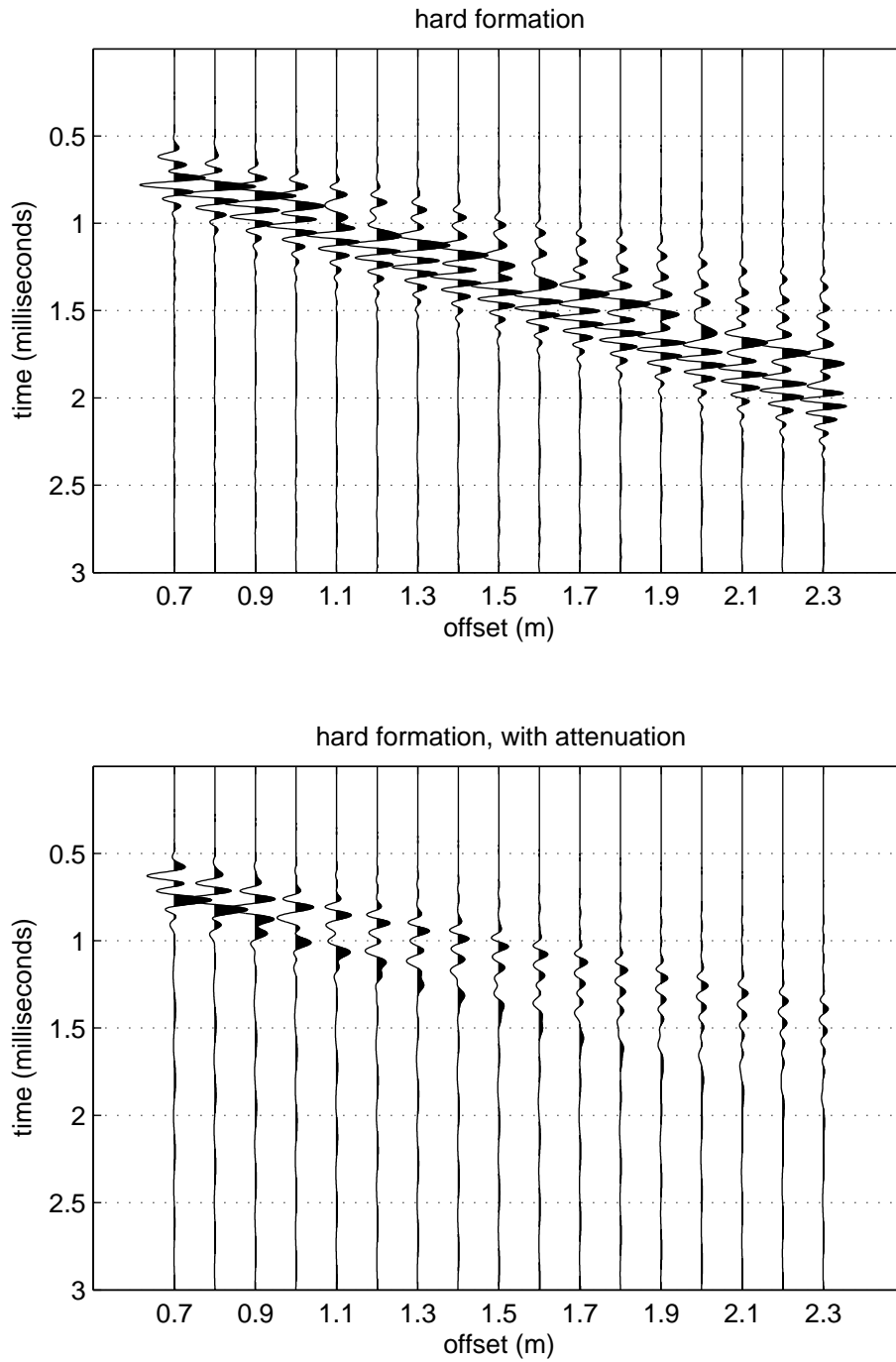


Figure 14: Results for models C1 and C2, the empty borehole in the hard formation. The amplitude scale is the same for the two plots. The high frequency guided waves are diminished by the attenuation.

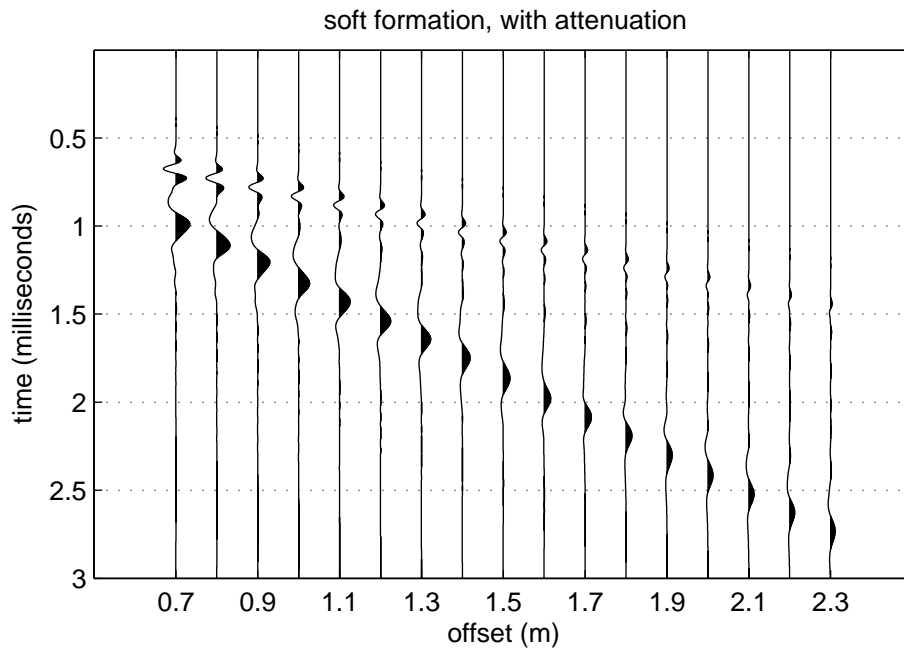
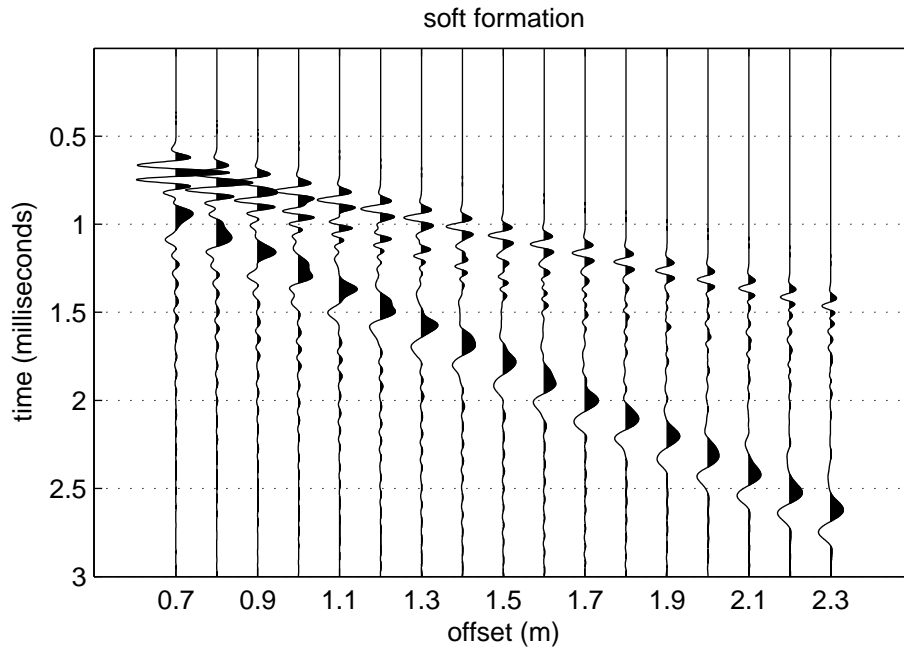


Figure 15: Results for models C3 and C4, the empty borehole in the soft formation. The high frequency guided waves have been attenuated out. The bottom plot has the amplitudes scaled by a factor of four relative to the top plot so that the events will be visible.